ACS APPLIED ENERGY MATERIALS

Article

All-Inorganic CsPbBr Nanocrystals: Gram-Scale Mechanochemical Synthesis and Selective Photocatalytic CO Reduction to Methane

Santosh Kumar, Miriam Regue, Mark Isaacs, Emma Freeman, and Salvador Eslava

ACS Appl. Energy Mater., **Just Accepted Manuscript** • DOI: 10.1021/acsaem.0c00195 • Publication Date (Web): 16 Apr 2020

Just Accepted

is published by the American Chemical Society. 1155 Sixteenth Street N.W., Washington, DC 20036

All-Inorganic $CsPbBr_3$ Nanocrystals: Gram-Scale Mechanochemical Synthesis and Selective Photocatalytic CO_2 Reduction to Methane

Santosh Kumar,[†,§] Miriam Regue,[†,‡,§] Mark A. Isaacs,[+] Emma Freeman,[†] and Salvador Eslava[*,†,§]

[†] *Department of Chemical Engineering, Imperial College London, London, SW7 2AZ, United Kingdom*

[§] *Department of Chemical Engineering, University of Bath, Claverton Down, Bath, BA2 7AY, United Kingdom*

[‡] *Centre for Sustainable Chemical Technologies, University of Bath, Claverton Down, Bath, BA2 7AY, United Kingdom*

[+] *Department of Chemistry, University College London, London, WC1H 0AJ, United Kingdom*

* Corresponding author. E-mail: s.eslava@imperial.ac.uk

KEYWORDS: Halide perovskite, photocatalysis, CO_2 reduction, graphene oxide, heterojunction

ABSTRACT: Halide perovskite $CsPbBr_3$ has recently gained wide interest for its application in solar cells, optoelectronics and artificial photosynthesis, but further progress is needed to develop greener and more scalable synthesis procedures and for their application in humid environments. Herein, we report a fast and convenient mechanochemical synthesis of $CsPbBr_3$ perovskite nanocrystals with control over crystal size and morphology. These perovskite

nanocrystals show excellent crystallinity and tunable morphologies, from nanorods to nanospheres and nanosheets, simply changing the mechanochemical reaction conditions such as ball milling time, ball size and Cs precursor. Furthermore, we explore their use for gas-phase photocatalytic CO_2 reduction using water vapor as proton source. A photocatalytic conversion of CO_2 and H_2O(g) to 0.43 (±0.03) μmol CH_4 g^{-1} h^{-1}, 2.25 (±0.09) μmol CO g^{-1} h^{-1} and 0.08 (±0.02) μmol H_2 g^{-1} h^{-1} was for example achieved with $CsPbBr_3$ nanosheets and simulated sunlight, keeping 30% of this activity over three consecutive cycles. When these $CsPbBr_3$ nanosheets were mechanochemically prepared together with Cu-loaded reduced graphene oxide (Cu-RGO), the photocatalytic activity significantly improved to 12.7 (±0.95) μmol CH_4 g^{-1} h^{-1}, 0.46 (±0.11) μmol CO g^{-1} h^{-1} and 0.27 (±0.02) μmol H_2 g^{-1} h^{-1}, and a 90% of this activity was retained over three consecutive cycles. The selectivity for CH_4 increased to 98.5(±0.93)% on an electron basis and a remarkable apparent quantum efficiency of 1.10(±0.15)% at 523 nm was achieved. This enhanced activity, selectivity and stability were assigned to the better charge separation, visible light absorption, CO_2 adsorption & activation, and hydrophobic character of the obtained composites. These results will contribute to the rational design and application of halide perovskites for CO_2 photocatalytic reduction.

INTRODUCTION

The artificial photosynthesis of carbon-based solar fuels using CO_2 as a feedstock has gained tremendous attention in recent years. This technology would provide clean fuels for vehicles and feedstocks for the chemical industry and simultaneously help to mitigate the global climate change caused by rising anthropogenic CO_2 in the atmosphere.[1-2] For this purpose, many different photocatalysts have been researched to absorb the solar spectrum, for example Cu_2O,[3] g-C_3N_4,[4] h-BN,[5] and CdS,[6] including different heterojunctions such as Bi_2WO_6/RGO/g-C_3N_4.[7] However, further progress is needed to efficiently reduce CO_2 in gas photocatalytic reactors,

tackling the limitations of most photocatalysts, namely poor light absorption, low CO_2 adsorption, poor separation and transfer of photoinduced charges, and poor selectivity for certain carbon-based products such as CH_4 or CO.[8]

In recent years, due to their high extinction coefficients, visible-light absorption and long electron and hole diffusion lengths, halide perovskites have emerged as promising materials for optoelectronic applications, especially in photovoltaic devices with a current record power conversion efficiency above 25%.[9-12] These halide perovskite materials have also been investigated in the field of photocatalysis, including H_2 evolution and CO_2 reduction. For example, all-inorganic $CsPbX_3$ (X: halide) perovskites have proven to be successful for photocatalytic CO_2 reduction, especially $CsPbBr_3$ perovskite. $CsPbBr_3$ quantum dots photocatalytically reduced CO_2 to CO and CH_4, with a production of 4.3 and 1.5 μmol g^{-1} h^{-1}, respectively.[13] Tuning the halide ratio to $CsPb(Br_{0.5}/Cl_{0.5})_3$ enhanced 5.9 and 4.9 times the photocatalytic CO_2 reduction to CO (85 μmol g^{-1} h^{-1}) and CH_4 (12 μmol g^{-1} h^{-1}) when compared with pristine $CsPbBr_3$ and $CsPbCl_3$.[14] Composites with $CsPbBr_3$ quantum dots have also been prepared. For example, $CsPbBr_3$ quantum dots combined with reduced graphene oxide (RGO) showed a photocatalytic activity for CO_2 reduction to CO and CH_4 of 4.80 and 2.46 μmol g^{-1} h^{-1}, respectively, with a 77% selectivity for CO.[15] Other composites used metal organic frameworks (MOFs) such as a zeolitic imidazolate framework ZIF-67 to protect the halide perovskite from decomposition and to enhance its photocatalytic activity for CO_2 reduction to CO and CH_4 – for example the major product CH_4 increased from 0.5 to 3.43 μmol g^{-1} h^{-1}.[16] Other examples of $CsPbBr_3$-based photocatalysts included other types of MOFs such as UiO-66(NH_2)[17], iron-based MOFs,[18] and graphitic carbon nitride (g-C_3N_4).[19] Unfortunately, these CO_2 photocatalytic studies using $CsPbBr_3$ use an organic solvent (ethyl acetate or acetonitrile) as a reaction medium where water and CO_2 are dissolved. Such use of a slurry photocatalytic reactor with organic solvents for the CO_2 conversion limits the yields and scale-up to the

solubility of CO_2 in the solvent used. Moreover, most studies have been limited to $CsPbBr_3$ quantum dots stabilised with surfactants, lacking a more extended study on pure halide perovskite crystals.

All-inorganic halide perovskites, particularly $CsPbBr_3$ nanocrystals and quantum dots, have often been prepared using organic solvent-intensive multistep reactions with carcinogenic surfactants and ligands, which also limit their application and scale-up.[20-22] It is therefore important to develop alternative greener approaches with scale-up capability such as mechanochemical synthesis, also known as ball milling, that avoids or minimizes the use of organic solvents.[23-27] A few reports have covered the mechanochemical synthesis of organic-inorganic halide perovskites,[23-25] double halide perovskites, [26] and $CsPbBr_3$ quantum dots.[27] Further progress is still needed on the mechanochemical synthesis of all-inorganic halide perovskite nanocrystals such as $CsPbBr_3$ with control over size and morphology.

In this paper, we demonstrate efficient and reproducible gram-scale mechanochemical syntheses of all-inorganic $CsPbBr_3$ perovskite nanocrystals with nanorod, nanosphere or nanosheet shapes. Their nanocrystal size and properties were finely tuned by changing the mechanochemical reaction conditions such as ball milling time, ball size, and Cs precursor. Importantly, we also demonstrate these $CsPbBr_3$ perovskite nanocrystals were photocatalytically active for gas-phase CO_2 + H_2O(g) conversion to CH_4, CO, H_2 and O_2 products with simulated sunlight. Furthermore, when $CsPbBr_3$ nanosheets were mechanochemically synthesized with Cu-loaded RGO, the heterostructure exhibited remarkable improvement in the selective photocatalytic CO_2 reduction to CH_4, achieving 12.7 (±0.95) μmol CH_4 g^{-1} h^{-1} and 98.5(±0.93)% CH_4 selectivity, with apparent quantum efficiency of 1.10(±0.15)% at 523 nm.

EXPERIMENTAL DETAILS

Materials and methods:

$PbBr_2$ (98%, Sigma-Aldrich), Cs_2CO_3 (99%, Alfa Aesar), CsOAc (CH_3COOCs, 99.999%, Alfa Aesar), CsBr (99.9%, Acros Organics), ethylene glycol (99%, Acros Organics), isopropanol (99.7%, VWR Chemicals) and hexane (HPLC grade, Fisher) used in this work are of analytical grade and used as received.

All $CsPbBr_3$ nanocrystals were synthesized by mechanochemical synthesis. For the preparation of $CsPbBr_3$ nanorods (NR) and nanospheres, 2 mmol of CsOAc and 3 mmol of $PbBr_2$ were added to a 45-mL zirconia bowl containing zirconia balls under a controlled atmosphere in a glove box (< 1 ppm H_2O, < 3 ppm O_2). Either 180 zirconia balls of 5 mm diameter or 18 zirconia balls of 15 mm diameter were used. The gas-tight zirconia bowl with zirconia balls and Cs and Pb precursors was then placed in a ball-milling machine (Planetary Mono Mill Pulverisette, Fritsch) and milled at 500 rpm for 60, 180 or 300 min. Then, the as-prepared $CsPbBr_3$ nanocrystals were, in the natural laboratory atmosphere outside the glove box, dispersed in 10 mL of isopropanol and centrifuged at 3,000 rpm for 5 min, repeating this washing step three times with isopropanol and once with n-hexane before drying overnight in dry nitrogen gas. All these resulting nanocrystals had NR shape, except for 300 min ball milling which resulted in nanospheres. Products weighted □1.1 g (95 wt% yield). Samples were, eventually, stored in closed vials within an Ar glove box, unless differently specified for stability studies.

For the preparation of $CsPbBr_3$ nanosheets (NS), 1 mmol of CsBr and 1 mmol of $PbBr_2$ were used as Cs and Pb precursors, respectively, together with 180 zirconia balls of 5 mm diameter. Ball milling was carried out for 180 min at 500 rpm. For the collection of the product, the balls were washed twice with 10 mL of isopropanol, centrifuged at 300 rpm for 5 min, and dried under vacuum. Samples weighted 0.56 g (97 wt% yield).

Graphene oxide (GO) was prepared by using a modified Hummer's method previously reported by Eslava *et al*.[28] Cu-RGO nanocomposites were prepared by a solvothermal method with the assistance of ethylene glycol (EG) as a reducing agent. Specifically, 4.75 mg of $Cu(NO_3)_2 \cdot 6H_2O$ and 25 mg of GO were dispersed in EG using ultra-sonication for 10 min. The resultant suspension was solvothermally treated in a 50 ml sealed Teflon-lined autoclave at 180°C for 24 h. The precipitates were washed with isopropanol and re-dispersed again in isopropanol to a final concentration of 2 mg mL^{-1}. The content of Cu in the Cu-RGO solid was approximately 5 wt%, which was found optimal. Pure RGO was prepared in the same way in the absence of Cu precursor.

Composites of $CsPbBr_3$ and either Cu-RGO or RGO were prepared by adding 5 ml of either Cu-RGO or RGO isopropanol suspensions (2 mg/ml in case of NR or 1 mg/ml in case of NS) to the previously described $CsPbBr_3$ nanocrystal syntheses before ball milling. *Ex-situ* synthesis of $CsPbBr_3$ and Cu-RGO composites were also prepared by mixing 0.2 g of $CsPbBr_3$ nanocrystals and 1 ml of Cu-RGO isopropanol suspension (2 mg/ml) with 20 ml of isopropanol, stirring at room temperature for 2 h, and finally evaporating the isopropanol at 60 ^oC under stirring. RGO was approximately 1 wt% in all the $CsPbBr_3$-RGO composites, which is known to be optimal in RGO-photocatalyst composites.[29] A physical mixture of $CsPbBr_3$ and Cu-RGO was also prepared by simply mixing the powders in the same mass ratio.

Characterization:

Powder X-ray diffraction (XRD) was carried out in a Bruker-AXS D8 ADVANCE diffractometer operated at 40 kV voltage and 40 mA current using Cu Kα (λ = 0.15418 nm) radiation in the 2θ range 5–80°. Surface analysis was performed by X-ray photoelectron spectroscopy (XPS) using a Kratos Axis HSi spectrometer and monochromated Al Kα X-ray source operated at 90 W. Binding energies were referenced relative to adventitious carbon at 284.6 eV. Spectral processing was performed using CasaXPS version 2.3.16. Catalyst morphology and crystallinity were investigated by high-resolution transmission electron microscopy (HRTEM) using a JEOL JEM-2100Plus microscope operating at an accelerating voltage of 200 kV. Energy dispersive X-ray spectroscopy (EDX) was used for mapping analysis of the elemental distribution through an Oxford INCA X-ray analyzer. Light absorption was measured by UV-visible diffuse reflectance spectroscopy (UV-Vis DRS) on a Cary 100 spectrophotometer (Agilent Technologies) using an integrating sphere for diffuse reflectance and KBr as a standard. Baseline was corrected using pure KBr and then 10 mg of sample were mixed with KBr for analysis. The band gap energy (E_g) of all the $CsPbBr_3$ samples was determined using Tauc plots of $[F(R)h\nu]^{1/n}$ versus $h\nu$ and drawing a tangential line at the onset,[30] where $F(R)$, $h\nu$, and η are Kubelka-Munk function, energy of light, and a variable that depends on the nature of the optical transition during photon absorption (equal to 1/2 in this case), respectively. $F(R)$ was calculated as $F(R)=(1-R)^2(2R)^{-1}$, where R is the reflectance of the sample.[30] Steady-state photoluminescence (PL) spectra were recorded on a Cary Eclipse fluorescence spectrophotometer (Agilent Technologies) at an excitation wavelength of 365 nm. Each PL spectrum was individually normalized by the mass of the sample. Nitrogen and CO_2 adsorption measurements were performed with a Quantachrome Autosorb IQ_2 porosimeter. Surface areas were calculated over the nitrogen relative pressure range 0.01–0.2 using Brunauer–Emmett–Teller (BET) model.

Photocatalysis:

Photocatalytic CO_2 reduction with prepared photocatalyst powders was carried out at room temperature in a gas-tight 125 ml glass photoreactor with top quartz light window. 1 sun in the powder sample was obtained using an AM 1.5G filtered 300 W Xe source at an appropriate distance to obtain 100 mW cm^{-2}, calibrated with a ILT1400 radiometer (International Light Technology). 50 mg of sample was placed in a glass holder within the photoreactor. Prior to irradiation, the reactor was purged with He gas to remove air from the system and then purged with CO_2 for 1 h at 5 ml min^{-1} humidified by injecting water at 1 ml h^{-1} simultaneously with a high-precision pump. The relative humidity observed by a dew point meter HT-6292 from Landtek was 57.5%. Subsequently, the gas inlet and outlet in the reactor were closed in this order to keep atmospheric pressure and then the photocatalysis was carried out by irradiating for 4 h. The gas products were analyzed by gas chromatography (GC, Shimadzu GC-2030 Plus) with He as a carrier gas and a barrier ionization detector (BID). Any small air leak in the system during the experiments was identified and quantified using the N_2 peak and assuming 21% O_2 and 79% N_2 in air. No liquid products were observed in the given experimental conditions. Reusability experiments were carried out for three consecutive runs on the same samples by each time degassing with He, followed by purging with fresh CO_2 and water vapor, and then irradiating for 4 h (12 h of total irradiation). The error bars in charts and the ± symbol in the text indicate standard deviation. The selectivity of the gas products on an electron basis was calculated with the following equations:[31]

$$\text{Selectivity for CO production (\%)} = \frac{2N_{CO}}{8N_{CH_4} + 2N_{CO} + 2N_{H_2}} \text{x } 100 \qquad (1)$$

$$\text{Selectivity for } CH_4 \text{ production (\%)} = \frac{8N_{CH_4}}{8N_{CH_4} + 2N_{CO} + 2N_{H_2}} \text{ x } 100 \qquad (2)$$

$$\text{Selectivity for } H_2 \text{ production } (\%) = \frac{2N_{H_2}}{8N_{CH_4} + 2N_{CO} + 2N_{H_2}} \text{x } 100 \quad (3)$$

where N_{CH_4}, N_{CO}, and N_{H_2} are the production rates of CH_4, CO, and H_2 in μmol g^{-1} h^{-1} and the coefficients 8, 2 and 2 are used to account for the electrons involved in the reduction reactions to form CH_4, CO and H_2, respectively. The apparent quantum efficiency (AQE) was measured using the same experimental setup, but with 523 nm LED light source to obtain monochromatic light and the following equation:

$$\text{AQE } (\%) = \frac{\text{Number of reacted electrons}}{\text{Number of incident photons}} \times 100 \quad (4)$$

Further details of the AQE calculations are given in the electronic supplementary information.

RESULTS AND DISCUSSION

Synthesis:

The general pathway used to prepare $CsPbBr_3$ nanocrystals was a surfactant-free mechanochemical synthesis (**Scheme 1**). During milling, the kinetic energy of the balls was transferred to both Cs and Pb precursors allowing their collision and chemical reaction to form $CsPbBr_3$ nanocrystals, as shown in the following equation for the use of CsOAc as a reactant**:**[32]

$$2\ CsOAc + 3\ PbBr_2 \rightarrow 2\ CsPbBr_3 + Pb(OAc)_2 \quad (5)$$

Pure $CsPbBr_3$ nanocrystals following **Equation (5)** were obtained for a minimum of 1 h ball-milling time at 500 rpm and after work-up to remove $Pb(OAc)_2$ byproduct. Their morphology and crystal structure were investigated by TEM and HRTEM. $CsPbBr_3$ nanocrystals

showed rod-like morphologies with a diameter of 60-70 nm and a length of a few hundred nm (**Figure S1a and Figure 1(a, d)**). Metal acetate precursors often favor anisotropic growth, which would explain the rod-like morphology.[33] Clear lattice fringes with an interplanar spacing of 0.41 nm were assigned to the (110) plane of the orthorhombic $CsPbBr_3$ phase (**Figure S1b**).[22] A selected angle electron diffraction (SAED) pattern further confirmed their crystallinity and orthorhombic $CsPbBr_3$ phase (**Figure S1c**).[34] EDX spectra showed that the nanorods were composed of Cs, Pb, and Br elements in a 1:1:3 average ratio (**Figure S1d**).

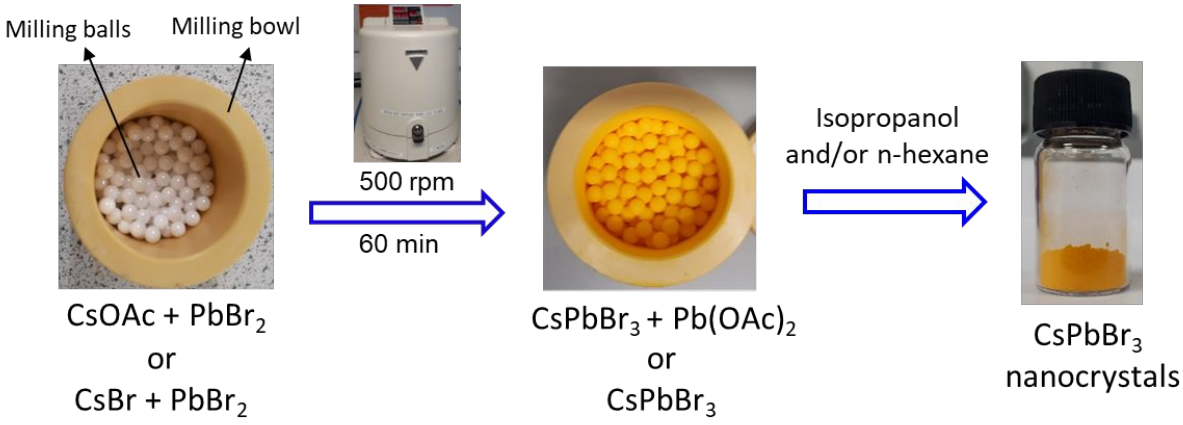

Scheme 1: Schematic diagram of the $CsPbBr_3$ nanocrystals synthesis by a surfactant-free mechanochemical synthesis method.

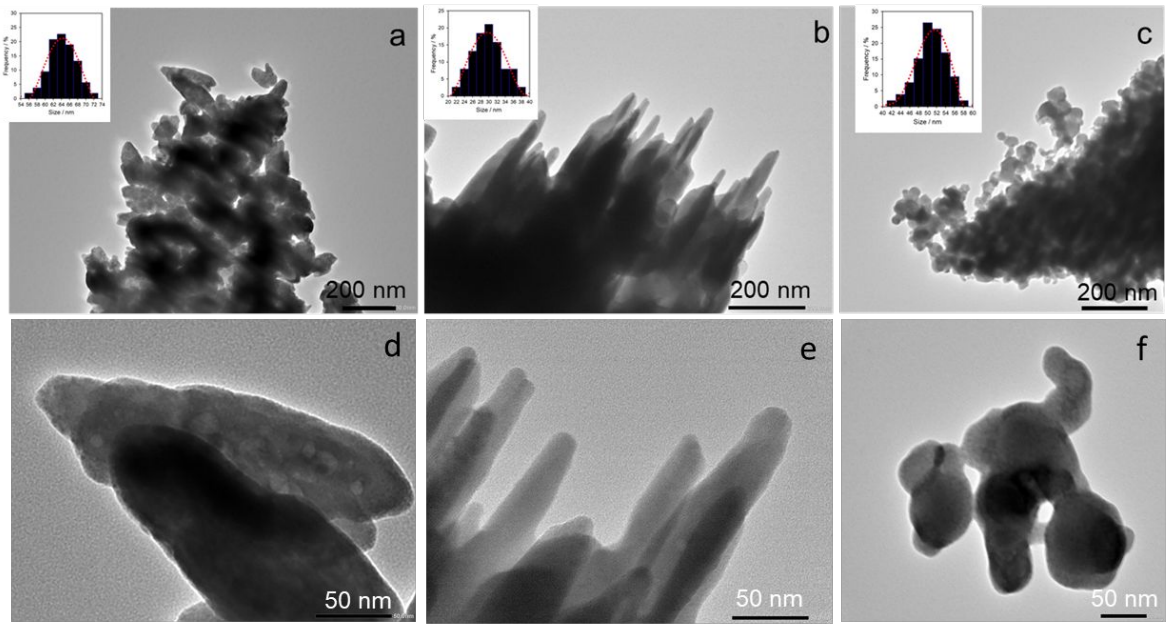

Figure 1. TEM micrographs of nanorods and nanospheres prepared using CsOAc, 500 rpm and 5 mm diameter zirconia balls for (a, d) 60, (b, e) 180, and (c, f) 300 min of ball milling. Inset charts show their size distribution.

Ball-milling time effect:

The influence of the ball-milling time on the size and morphology of $CsPbBr_3$ nanocrystals prepared with CsOAc was assessed. When ball-milling time increased from 60 to 180 min, the nanorod structure remained the same but the diameter of the nanorods decreased from 60-70 to 20-40 nm (**Figure 2(b, e)**). For a longer ball milling of 300 min, the morphology changed from nanorod to nanosphere shape, with a diameter of 40-50 nm (**Figure 2(c, f)**). This morphology evolution was attributed to the different amounts of energy received for different time periods of mechano-chemical synthesis, where rods initially formed and after some time deformed to rounded shapes. A similar evolution with an increasing synthesis temperature was observed in ZnO crystals prepared by mechanical-assisted thermal decomposition of zinc acetate.[33] These results revealed that morphology and shape can easily be controlled with ball-milling time. XRD confirmed the formation and conservation of the crystalline $CsPbBr_3$ prepared for different time periods (60-300 min, **Figure 2a**) and $Pb(OAc)_2$ as a by-product,

easily removed by washing with isopropanol **(Figure S2, Equation 5).**[35,36] The diffraction peaks at 15.20, 21.45, and 30.67° (2θ) in the XRD patterns of $CsPbBr_3$ products matched well with the (110), (112), and (220) planes of the orthorhombic $CsPbBr_3$ perovskite structure, respectively (PDF# 97851).[37]

UV-Vis DRS of $CsPbBr_3$ nanocrystals prepared with CsOAc and different ball milling time periods are shown in **Figure 2b**. A sharp absorption onset at 527 nm for all $CsPbBr_3$ nanocrystals confirmed a band gap of 2.35 eV (**Figure S3a-c**).[34] The band gap energy appeared independent of the size and morphology of the nanocrystals, since their dimensions above 30 nm avoid quantum effects typically observed in $CsPbBr_3$ quantum dots.[38] Consistent with the same band gap energy, the color appearance of all the nanocrystals was the same, as shown in photographs **(insets in Figure S3a-c)**. PL spectroscopy was used to study the charge carrier separation and transfer. All the steady-state PL emission spectra upon an excitation wavelength of 365 nm were similar and consisted of an emission located at ~530 nm, assigned to the band gap transition (**Figure 2c**).[15]

XPS was used to probe the chemical oxidation state of Cs, Pb, and Br and their chemical environment (**Figure 2d-f**). No relevant differences could be observed between samples prepared for different ball milling time. Representative high-resolution Cs 3d, Pb 4f and Br 3d XPS spectra showed peaks at 738.7, 724.8, 142.96, 138.10, 69.63 and 67.92 eV attributed to Cs $3d_{5/2}$, Cs $3d_{3/2}$, Pb $4f_{7/2}$, Pb $4f_{5/2}$, Br $3d_{7/2}$ and Br $3d_{5/2}$, respectively.[39] The energy distance between the valence-band (VB) edge potential and the Fermi level (E_f) was determined from VB XPS spectra, calculating the intercept between the tangent of the onset and the baseline of the spectra (**Figure S3d**). A value of approximately 1.60 eV was found, in agreement with literature.[40] The same XPS tool was used to measure the electronic workfunction, that is the

difference between E_f and the vacuum level, from an ultraviolet photoelectron spectrum (UPS). A value of approx. 4.39 eV was measured (Figure 3e).[41] Combining these values with the measured band gap energy of 2.35 eV, we constructed the energy diagram of these $CsPbBr_3$ materials, as shown in **Figure S3f**. The CB edge potential was calculated to be at –3.64 eV from the vacuum level. This value confirmed that photoinduced electrons on the $CsPbBr_3$ CB edge position will have suitable potential for multielectron CO_2 reduction potentials to various low-carbon chemical fuels, for example CO_2/CO (–0.53 V_{NHE} at pH = 7) and CO_2/CH_4 (– 0.24 V_{NHE} at pH = 7) (**Figure S3f**).

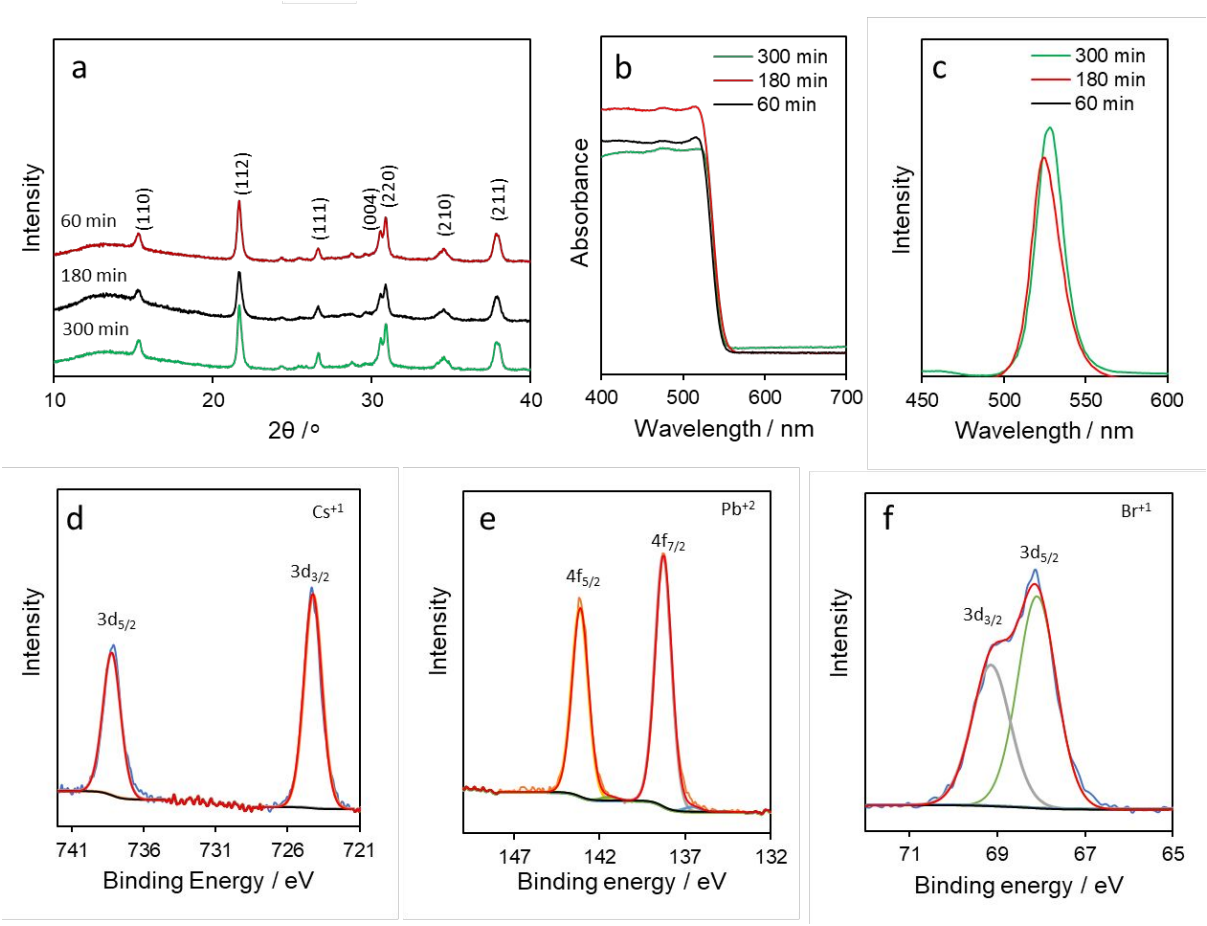

Figure 2. Characterization of $CsPbBr_3$ nanorods and nanospheres prepared for different ball-milling time periods using CsOAc, $PbBr_2$, 500 rpm and 5 mm diameter zirconia balls. (a) XRD

patterns. (b) UV-Vis DRS spectra. (c) Normalized PL spectra. Representative (d) Cs 3d, (e) Pb 4f and (f) Br 3d XPS spectra.

Milling ball size effect:

A second milling ball size was used to assess the ball influence on the final products. The 150 balls of 5 mm were replaced with 18 balls of 15 mm to keep the same overall mass of zirconia balls. The rest of conditions were kept for this analysis, that is 60 min ball milling that ensured pure product phase, 500 rpm and use of CsOAc and $PbBr_2$. The diameter of the rods stayed constant (60-70 nm) with the use of larger balls (**Figure 2a and 3a-b**). However, the length of the nanorods increased from a few hundred nm to a few μm, obtaining higher aspect ratio nanorods. The increase in aspect ratio with larger milling balls could be due to a much faster reaction rate under the stronger collision of larger and, therefore, heavier balls.[42] XRD patterns, HRTEM, and UV-vis DRS showed no differences (**Figure 3c-e**). Normalized PL spectrum again consisted of an emission peak at 527 nm, but the intensity of these high aspect ratio rods was slightly lower than their counterpart nanorods, which might be due to slower electron–hole recombination and improved charge carrier separation (**Figure 3f**).[43]

Cs precursor effect:

The Cs precursor CsOAc was replaced with CsBr to determine the Cs precursor effects on the final morphology and crystallinity of $CsPbBr_3$. A 1:1 molar ratio of $CsBr:PbBr_2$ was used to form $CsPbBr_3$, as follows:

$$CsBr + PbBr_2 \rightarrow CsPbBr_3 \quad (6)$$

Using CsBr as precursor resulted in the formation of nanosheets of 20-40 nm thickness and 300-1000 nm length (**Figure 4a-b**). HRTEM lattice fringes of 0.58 nm on the nanosheet flat facet were assigned to the (001) plane of the orthorhombic phase of $CsPbBr_3$ (**Figure 4c**).[44] SAED patterns on the nanosheets showed very clear diffraction spots, indicating their highly crystalline nature (**Figure S4**). EDX mapping showed that Cs, Pb, and Br elements were uniformly dispersed in the nanosheet structure, with an atomic ratio of 1:1:3, respectively (**Figure S5**). XRD of $CsPbBr_3$ nanosheets prepared with CsBr confirmed they are also pure orthorhombic phase with no additional crystal phases (**Figure 4d**). UV−Vis DRS and PL spectroscopy showed no difference compared to the nanorods prepared with CsOAc (**Figure 4e-f)**. Furthermore, $CsPbBr_3$ mechanochemical synthesis was attempted with a third precursor for Cs, cesium carbonate Cs_2CO_3, with a Cs_2CO_3:$PbBr_2$ molar ratio of 1:3 and same conditions (500 rpm, 180 min, and 5 mm balls). Unfortunately, no pure $CsPbBr_3$ phase was formed, but a mixture of Cs_4PbBr_6 and orthorhombic $CsPbBr_3$ phases along with precursors (Cs_2CO_3 and $PbBr_2$) (**Figure S6**). We attributed the incomplete reaction to the lower reactivity of Cs_2CO_3, which requires substitution of the carbonate for other functional groups.[45]

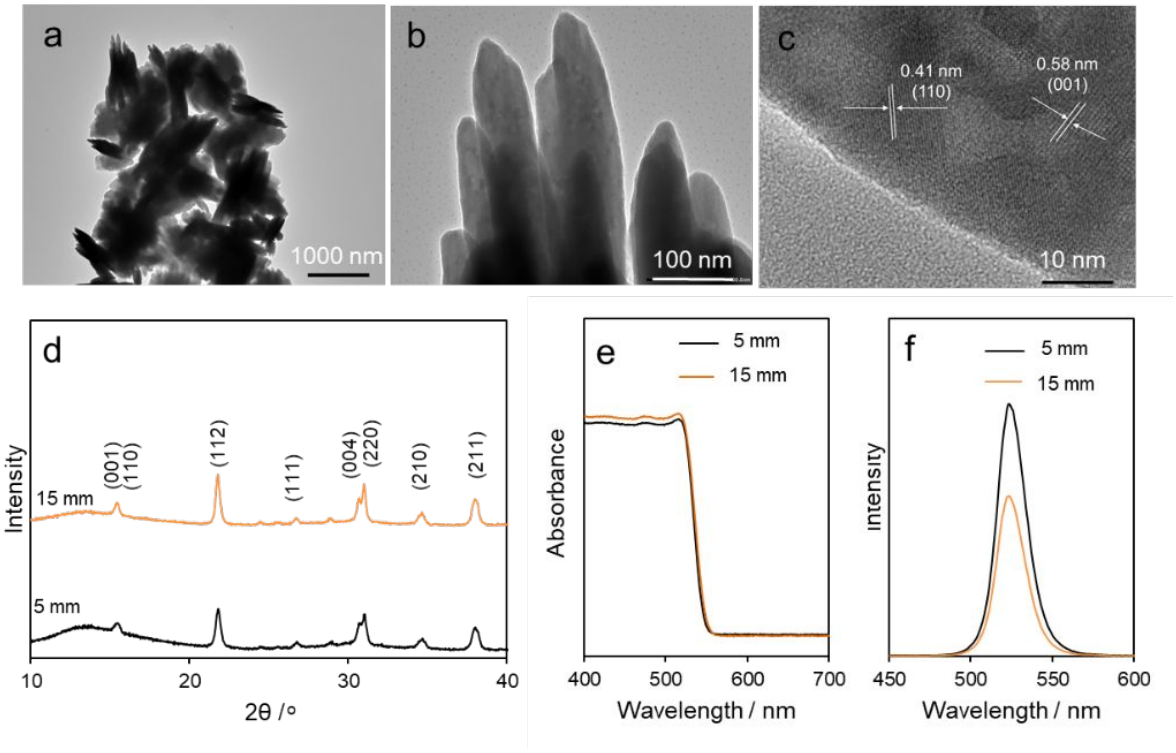

Figure 3. Characterization of $CsPbBr_3$ nanorods prepared by ball milling for 60 min using CsOAc, $PbBr_2$, 500 rpm and 15 mm zirconia balls (18 balls), compared with the use of 5 mm zirconia balls (180 balls). (a-b) TEM and (c) HRTEM micrographs of $CsPbBr_3$ nanorods prepared with 15 mm balls. (d) XRD, (e) UV-Vis DRS and (f) Normalized PL spectra of $CsPbBr_3$ nanorods synthesised using 5 mm and 15 mm balls.

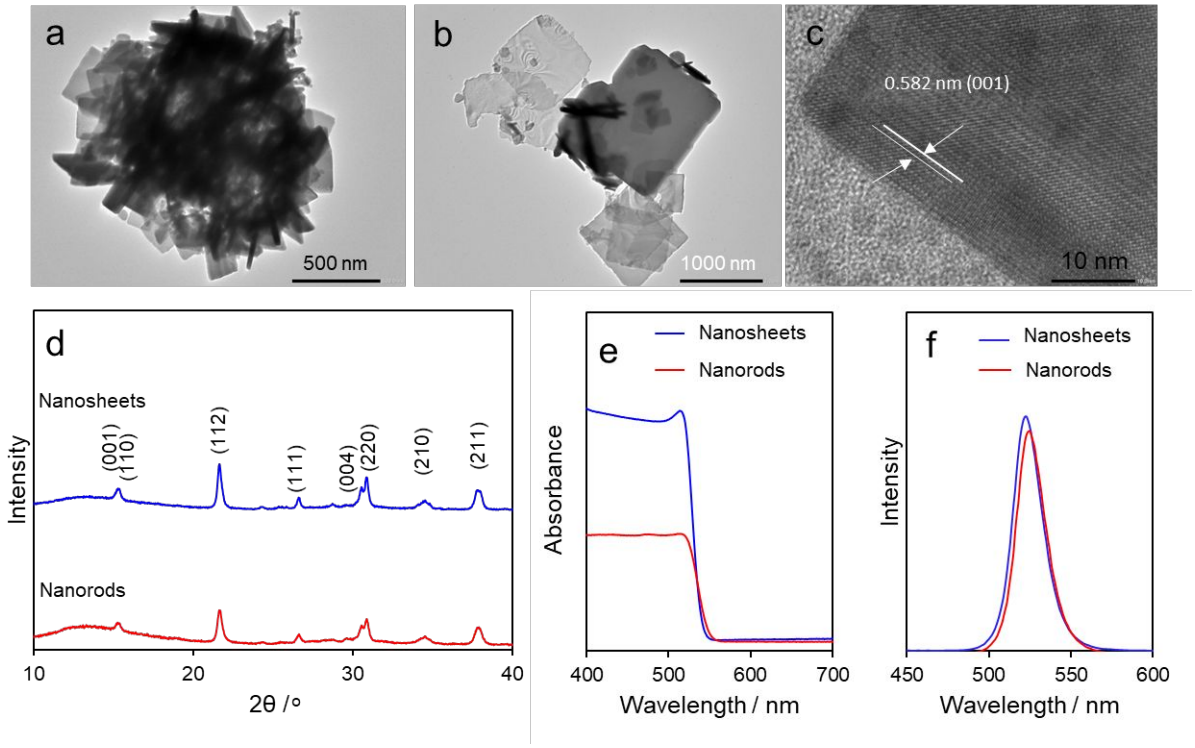

Figure 4. Characterization of $CsPbBr_3$ nanosheets prepared by ball milling for 180 min using CsBr, $PbBr_2$, 500 rpm and 5 mm zirconia balls, compared with the nanorods obtained with use of CsOAc in the same conditions. (a-b) TEM and (c) HRTEM micrographs of $CsPbBr_3$ nanosheets. (d) XRD patterns, (e) UV-Vis DRS and (f) Normalized PL spectra of $CsPbBr_3$ nanosheets compared with nanorods.

Chemical stability:

We investigated the stability of the $CsPbBr_3$ nanosheets under normal laboratory conditions with an observed relative humidity of 55-60%. Vials containing dried $CsPbBr_3$ nanosheets were opened in the lab environment and XRD diffraction patterns were measured at different time periods (**Figure S7**). Interestingly, no phase change was observed for 2 days, which indicates that $CsPbBr_3$ nanosheets were relatively stable in humid conditions. However, the coherent diffraction domain size increased from 21 to 39 nm, so perovskite crystals sintered during

exposure to humid ambient. After one week exposure to the humid lab ambient, $CsPbBr_3$ nanosheets decomposed to $PbBr_2$ and Cs_4PbBr_6 (**Figure S7a**).[46] Other $CsPbBr_3$ pure nanocrystals prepared under different conditions showed similar stability.

$CsPbBr_3$-Cu-RGO composites characterization:

Composites of $CsPbBr_3$ with Cu and RGO were prepared by mechanochemical synthesis to expand the properties of final products. XRD patterns of GO, RGO, Cu-RGO, NS-RGO (NS: $CsPbBr_3$ nanosheets) and NS-Cu-RGO samples are shown in **Figure 5a**. The characteristic diffraction peak of GO was observed at 11° (2θ). After reduction to RGO involving a substantial loss of oxygen functional groups, the interlayer spacing decreased resulting in broad diffraction peaks centered at 24 and 43° (2θ), corresponding to (002) and (100) planes of graphitic materials.[47] Composites containing $CsPbBr_3$ nanosheets diffracted according to the same pure orthorhombic phase, revealing that the addition of RGO or Cu-RGO suspensions did not affect the perovskite crystallinity phase resulting from the mechanochemical synthesis. No diffraction peaks assigned to Cu particles were observed in Cu heterostructures, indicating good dispersion and minute particle dimension. The characteristic Raman D and G bands around 1360 and 1620 cm^{-1} was observed in GO, RGO, Cu-RGO and NS-Cu-RGO samples, assigned to sp^3 defects and in-plane vibrations of sp^2 carbon atoms, respectively (**Figure 5b**).[48] The D band remained unchanged in GO and RGO samples, while the G band of RGO samples was slightly shifted to a lower wavenumber. This further confirmed the increased sp^2 character of RGO samples and therefore the reduction of GO to RGO.[48]

UV−Vis DRS absorption spectra of RGO, NS, NS-RGO, and NS-Cu-RGO nanocomposites are shown in **Figure 5c**. Spectra of nanocomposites containing nanosheets (NS) had an absorption onset, attributed to the $CsPbBr_3$ band gap of 527 nm (2.35 eV). The presence of

RGO shifted upwards the absorption baseline, since RGO absorbs broadly in the UV-vis region. The addition of Cu extended the visible absorption to higher wavelengths. PL emission spectra were collected for NS, NS-RGO, NS-Cu-RGO and *ex-situ*-NS-Cu-RGO samples, to assess the charge transfer between $CsPbBr_3$ and other phases (**Figure 5d**). The normalized PL intensity of the NS-RGO and NS-Cu-RGO nanocomposites was much lower than that of pure $CsPbBr_3$ nanosheets, which we attributed to photoinduced charge carriers separation between phases and suppressed electron–hole recombination. The normalized PL intensity of NS-Cu-RGO was also lower than that of *ex-situ*-NS-Cu-RGO, indicating the importance of good interfacing to achieve charge carriers separation between phases and suppressed electron–hole recombination (inset image of **Figure 5d**).

N_2 adsorption-desorption on NS, NS-Cu-RGO, and a physical mixture of NS and Cu-RGO were carried out to assess their porosity and surface area (**Figure 5e**). NS and the physical mixture showed type II isotherms, characteristic of non-porous materials.[49] NS-Cu-RGO showed type III hysteresis, probably due to the formation of slit-like pores within the aggregates of nanosheets.[49] NS-Cu-RGO nanocomposite (56 $m^2 g^{-1}$) had larger BET surface area than a simple physical mixture (44 $m^2 g^{-1}$) of its counterpart components in the same mass ratio. The optimal BET surface area of NS-Cu-RGO nanocomposite (56 $m^2 g^{-1}$) almost doubled that of NS (27 $m^2 g^{-1}$). CO_2 physisorption was carried out on the samples, since adsorption is very important in any heterogenous catalytic process (**Figure 5f**). $CsPbBr_3$ nanosheets (NS) physisorbed 3.0 $cm^3 g^{-1}$, while NS-RGO, physically mixed NS & Cu-RGO, and NS-Cu-RGO physisorbed 3.5, 3.9, and 4.7 $cm^3 g^{-1}$, respectively. Therefore, optimum CO_2 physisorption happened on NS-Cu-RGO, which was relatively much higher than its counterpart bare $CsPbBr_3$ nanosheets. We attributed the increased CO_2 physisorption in NS-Cu-RGO to the Cu-RGO presence. CO_2 can adsorb on Cu-RGO via π-π conjugation interactions and via the formation of surface-bound carbonate on hydroxyl groups (for example at RGO defects or Cu particles

surface).[50] Moreover, Cu-RGO can have a templating effect during the mechanochemical synthesis, spreading the precursors and eventually increasing the surface area of the final products[28, 50-52] Further investigation is required on the adsorption mode of CO_2 on $CsPbBr_3$ and the effect of water vapor, which probably involves the formation of bicarbonates and carbonic acid from surface or subsurface reactions of CO_2 and H_2O.[53] Very interestingly, vials containing NS-Cu-RGO were opened to expose the sample to the 55-60 % relative humidity in the lab air and no phase change was observed after 8 days, which indicated that the NS-Cu-RGO was relatively more stable in humid conditions than $CsPbBr_3$ nanosheets alone that decomposed to $PbBr_2$ and Cs_4PbBr_6 in the same conditions (Figure S7a-b). However, growth of the coherent diffraction domain sizes of the perovskite in NS-Cu-RGO still occurred during exposure to humid ambient like in $CsPbBr_3$ nanosheets alone.

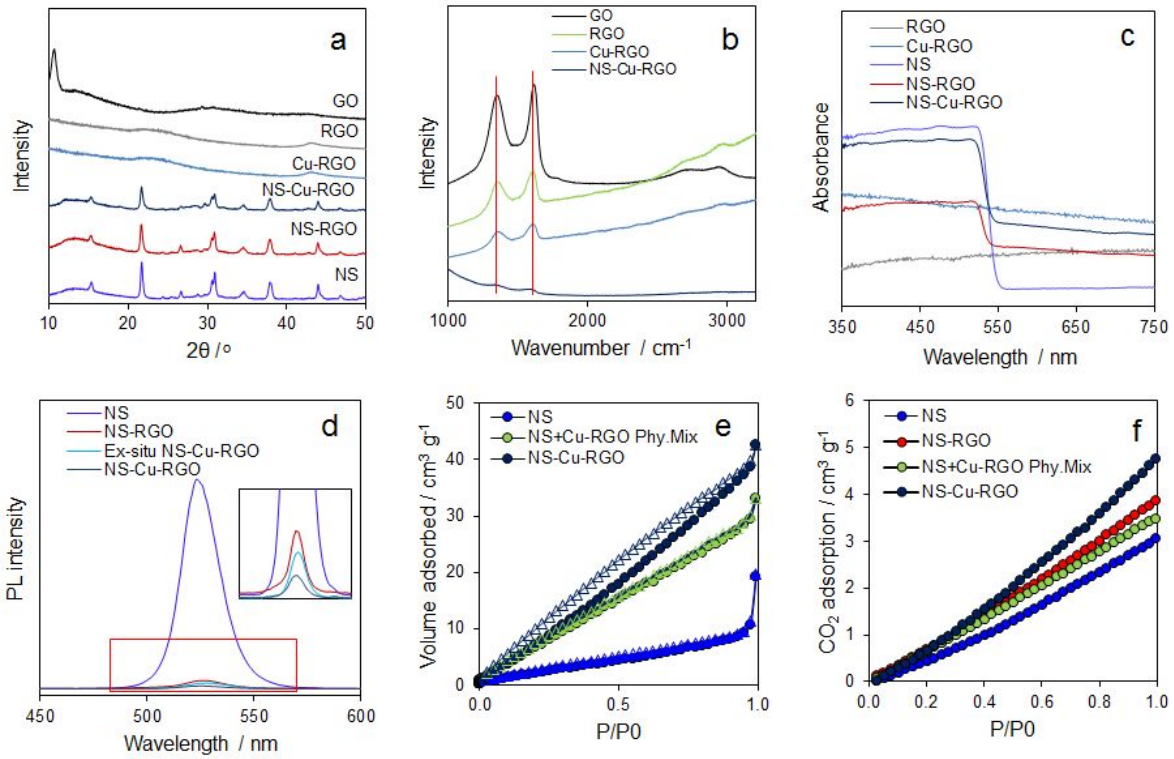

Figure 5. Characterization of $CsPbBr_3$ nanosheet composites prepared by ball milling for 180 min using CsBr, $PbBr_2$, RGO or Cu-RGO suspension, 500 rpm and 5 mm zirconia balls,

compared with individual components. (a) XRD patterns, (b) Raman spectra, (c) UV-Vis DRS absorbance spectra, (d) Normalized PL spectra, (e) N_2-adsorption-desorption isotherms (• ads, ∆ des) and (f) CO_2 adsorption at 298K. 'NS' in legends stands for 'nanosheets'.

RGO consisted of a layered structure with typical wrinkled surfaces (**Figure S8**). The two-dimensional RGO nanosheets tended to re-stack when dried due to van der Waals (vdW) interlayer interactions. After hybridisation with Cu nanoparticles in Cu-RGO, the typical wrinkled surface remained (**Figure 6a**). Cu nanoparticles were 4 nm in diameter and uniformly dispersed on the RGO surface (**Figure 6b**). Lattice fringes of 0.208 nm were observed, assigned to Cu (111) plane (**Figure 6c**). In NS-Cu-RGO composites, the $CsPbBr_3$ nanosheets grew much smaller around the Cu-RGO, with a thickness of 20-30 nm and a length of 100-500 nm, compared with 20-40 nm and 300-1000 nm in bare NS, respectively (**Figure 6d-e and 4a-b**). HR-TEM micrographs revealed intimate contact between the $CsPbBr_3$ nanosheets and Cu-RGO (**Figure 6f**). EDX mapping showed Cs, Pb, Br, C and Cu uniformly dispersed in the nanosheet structures (**Figure S9**). The percentage of Cu calculated by EDX was 0.2 wt%, whereas RGO was 1 wt% based on the amount used in the synthesis.

The hydrophilicity of the materials was investigated by water contact-angle measurement, since this property will affect the water vapor adsorption and photocatalytic oxidation and, at the same time, the chemical stability of $CsPbBr_3$ (**Figure 6g**). Both $CsPbBr_3$ nanosheets and GO were significantly hydrophilic as water was completely spread out on them upon contact. On the other hand, RGO with a contact angle of 87(±2)º was of much more hydrophobic character due to the restored C sp2 basal planes. Cu-RGO and NS-Cu-RGO composites offered intermediate results: 69(±2) and 43(±3)º, respectively, in agreement with their composition. Therefore, the use of RGO in NS-Cu-RGO reduced the hydrophilic character of $CsPbBr_3$ NS but did not suppress it.

Photocatalytic CO_2 reduction on bare $CsPbBr_3$:

Photocatalytic CO_2 reduction in the presence of water vapor was carried out in a gas-phase photocatalytic reactor under simulated sunlight (1 sun) containing powders of $CsPbBr_3$ nanocrystals and their composites with RGO and Cu-RGO. No hole scavengers such as organic alcohols, often used in CO_2 photocatalytic reduction, were used.[54-55] All $CsPbBr_3$ nanocrystals were photocatalytically active for CO_2 + H_2O(g) conversion to CO (major carbon product), CH_4 (minor carbon product), and H_2 (minor product), with relatively high selectivity (>90%) for carbon products (CO & CH_4) over H_2 product (**Figure 7**). $CsPbBr_3$ prepared with CsOAc and different milling time periods (60-300 min) showed different photocatalytic activity, optimal upon ball milling for 180 min (**Figure 7a**). We attributed this difference to the different morphologies obtained — 60–70 nm nanorods upon 60 min ball milling, 20–40 nm nanorods upon 180 min, and 40–50 nm nanospheres upon 300 min (**Figure 2a-c**) — being optimal in terms of surface area at 180 min. $CsPbBr_3$ nanorods prepared with CsOAc and two different milling ball sizes (5 and 15 mm) also showed different photocatalytic activity, being 40% (±0.03) higher when 15 mm balls were used (**Figure 7b**). We attributed this to the better charge carrier separation obtained in the high-aspect-ratio nanorods prepared with 15 mm balls as confirmed by PL spectroscopy (**Figure 3f**). $CsPbBr_3$ nanocrystals prepared with different Cs precursors also performed differently (**Figure 7c**). The resulting nanorods and nanosheets obtained with CsOAc and CsBr produced a similar activity (a total of 9.04 (±0.07) and 8.13 (±0.12) μmol g^{-1} h^{-1}, resp., in electrons consumption), despite the relatively higher surface area of the nanosheets (27 over 15 m^2 g^{-1}, **Figure S10**). However, nanosheets offered higher selectivity for carbon products, 98% *vs*. 90%.

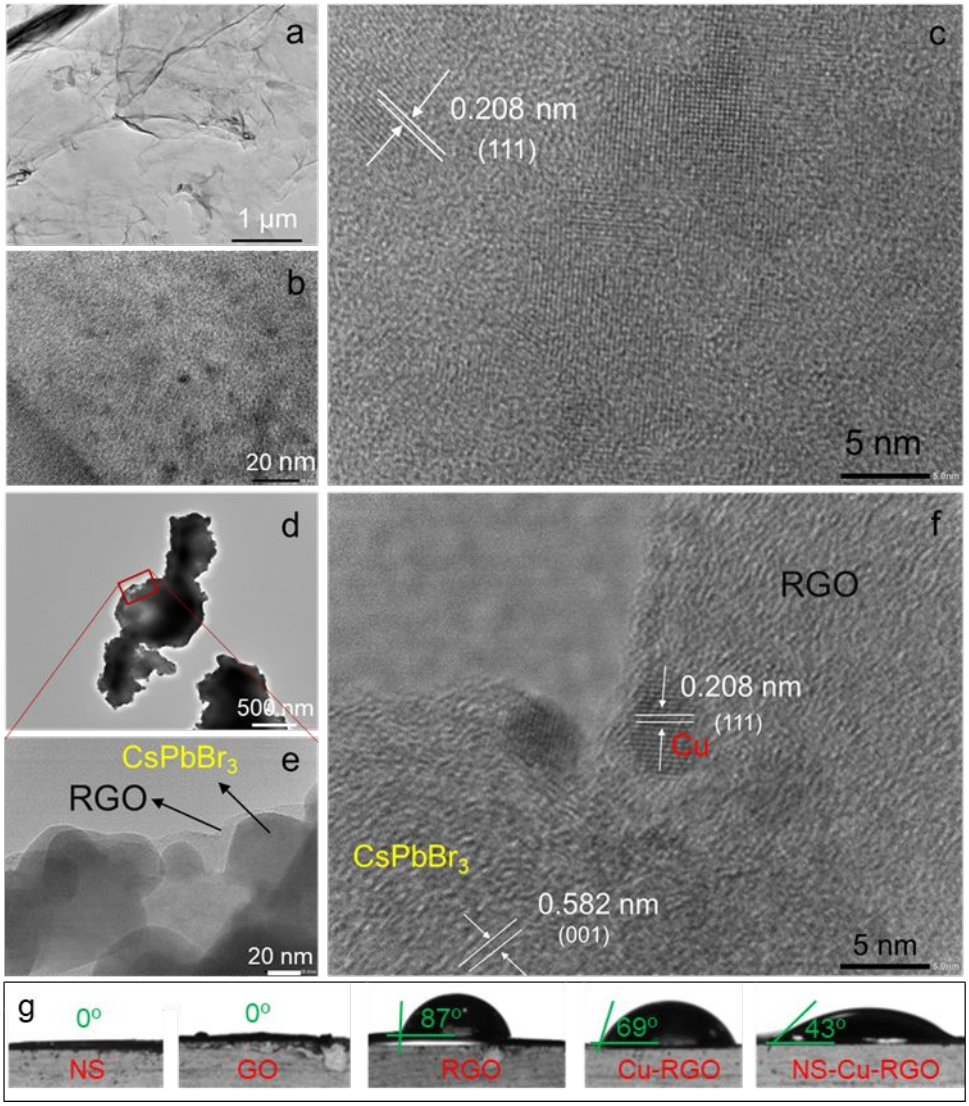

Figure 6. (a-b) TEM and (c) HRTEM micrographs of Cu-RGO. (d-e) TEM and (f) HRTEM micrographs of NS-Cu-RGO nanocomposite prepared by ball milling for 180 min using CsBr, $PbBr_2$, Cu-RGO suspension, 500 rpm and 5 mm zirconia balls. (g) Photographs of water contact angles.

For all the $CO_2 + H_2O$ (g) photocatalytic conversions we observed stoichiometric O_2 evolution, confirming the water oxidation on all the $CsPbBr_3$ nanocrystals (**Figure S11**). Using water is an advantage over the use of hole scavengers such as alcohols that would increase the costs of this technology.

Finally, we tested the performance stability of the nanosheets prepared with CsBr. The reactor gas mixture was evacuated and refilled with fresh gas reactant mixture for every repeated photocatalytic test. The $CsPbBr_3$ nanosheets were photocatalytically active during at least three consecutive cycles, although the production rates decreased 70% (**Figure 7d**). We attributed this decrease to the transformation of $CsPbBr_3$ to Cs_4PbBr_6 and $PbBr_2$ during the photocatalytic reaction conditions involving both simulated sunlight irradiation and water vapor, as confirmed by XRD (**Figure S12**)[46, 56] Control experiments were carried out on the same type of nanosheets in the absence of CO_2, H_2O, catalyst or light irradiation, in order to confirm the authenticity of the CO_2 + H_2O (g) photocatalytic conversion and reject any organic contamination contribution.[57-58] In all these control experiments, no CO or CH_4 were detected, except a small amount of H_2 in the absence of CO_2, confirming CO_2 as the carbon source and H_2O as the proton source (**Figure S13a**).

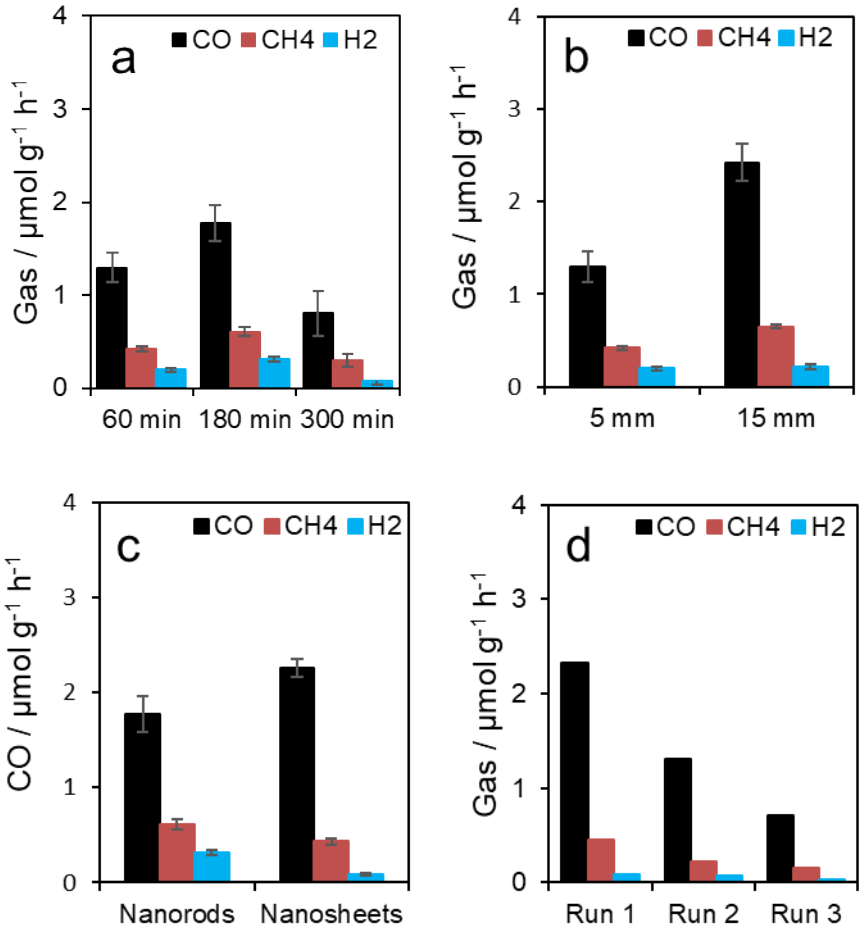

Figure 7. CO, CH_4, and H_2 production rates by photocatalytic CO_2 + H_2O (g) conversion measured on different $CsPbBr_3$ nanocrystals under 1 sun of simulated sunlight. (a) Ball milling time effect. $CsPbBr_3$ nanocrystals were prepared using CsOAc, $PbBr_2$, 500 rpm, 5 mm zirconia balls and different milling time periods. (b) Ball size effect. $CsPbBr_3$ nanocrystals were prepared using CsOAc, $PbBr_2$, 500 rpm, 60 min, and 5 or 15 mm zirconia balls. (c) Cs-precursor effect. $CsPbBr_3$ nanocrsystals were prepared with CsOAc (nanorods) or CsBr (nanosheets) for 180 min, 500 rpm, and 5 mm zirconia balls. (d) Stability tests. Reusability experiments on previous nanosheets for three consecutive runs.

Photocatalytic CO_2 reduction with composites of $CsPbBr_3$ and RGO or Cu-RGO:

The photocatalytic conversion of CO_2 and water vapor on composites of $CsPbBr_3$ nanocrystals and RGO or Cu-RGO were tested and compared (**Figure 8a-b**). The activity of $CsPbBr_3$ nanosheets (NS) prepared with CsBr and its RGO composite (NS-RGO) was similar to that of $CsPbBr_3$ nanosheets (NS) (**Figure 8a**). However, the composite NS-Cu-RGO achieved remarkable photocatalytic activity of 12.7 (±0.95) μmol CH_4 g^{-1} h^{-1}, 0.46 (±0.11) μmol CO g^{-1} h^{-1} and 0.27 (±0.02) μmol H_2 g^{-1} h^{-1}, much higher than NS: 0.43 (±0.03) μmol CH_4 g^{-1} h^{-1}, 2.25 (±0.09) μmol CO g^{-1} h^{-1} and 0.08 (±0.01) μmol H_2 g^{-1} h^{-1}. An also remarkable higher selectivity for CH_4 was obtained: 98.5 (±0.93)% CH_4, 0.9(±0.13)% CO, and 0.6(±0.02)% H_2 selectivity for NS-Cu-RGO compared with 42.5(±0.04)% CH_4, 55.4(±0.10)% CO, and 2.1(±0.02)% H_2 selectivity for NS. In terms of total electrons (e^-) consumption, NS-Cu-RGO achieved a photocatalytic activity of 103 (±0.98) μmol e^- h^{-1} g^{-1}, which is almost 13 times higher than NS (8.1 (±0.13) μmol e^- h^{-1} g^{-1}). We attributed this activity increase to the higher CO_2 adsorption and light absorption of NS-Cu-RGO, as observed in their characterization (**Figure 5c and 5f**), and to the presence of different phases in NS-Cu-RGO that favored charge separation and transfer and CO_2 activation. The intimacy between phases and quality of the interface was confirmed by PL spectroscopy (**Figure 5d**) and HRTEM (**Figure 6f**), but to further confirm its extent we also tested *ex-situ* NS-Cu-RGO and a physical mixture of NS and Cu-RGO (mixed powders). The photocatalytic activity of *ex-situ* NS-Cu-RGO (CH_4, 7.4 (±0.56) μmol h^{-1} g^{-1}) and specially the physical mixture NS+Cu-RGO (CH_4, 1.00 (±0.02) μmol h^{-1} g^{-1}) was poorer compared with the NS-Cu-RGO (CH_4, 12.7 (±0.95) μmol h^{-1} g^{-1}), which confirmed intimate and effective interfaces in the NS-Cu-RGO heterostructure.

The total O_2 evolved was correlated with a CH_4:O_2 and (CO+H_2):O_2 stoichiometry of 1:2 and 2:1, respectively, which was consistent with the involvement of 4 e^-, 8 e^-, 2 e^- and 2 e^- to form

O_2, CH_4, CO and H_2, resp. (**Figure S14**). The apparent quantum efficiency of CH_4 production using NS-Cu-RGO was calculated to describe the efficiency to absorb photons and drive photoinduced charges towards the production of solar fuels. The apparent quantum efficiency of NS-Cu-RGO was 1.10(±0.15)% at 523 nm, which was much higher than the efficiency reported for many heterogeneous photocatalysts (**Table S1**). Composites of Cu-RGO and $CsPbBr_3$ nanorods prepared with CsOAc also demonstrated high photocatalytic activity but slightly lower than that of $CsPbBr_3$ nanosheets prepared with CsBr (**Figure 8b**), which could be due to the morphology of the nanorods matching less with the RGO than the nanosheets. Finally, we checked the reusability of the most successful composite, the NS-Cu-RGO, crucial for its practical application. While nanosheets alone only retained 30% of its original photocatalytic activity for CO_2 conversion during three consecutive cycles (**Figure 7d**), NS-Cu-RGO nanocomposite retained almost 90% of its original photocatalytic activity **(Figure 8c)**. Control experiments were again carried out confirming CO_2 as the carbon source and H_2O as the proton source (**Figure S13b**).

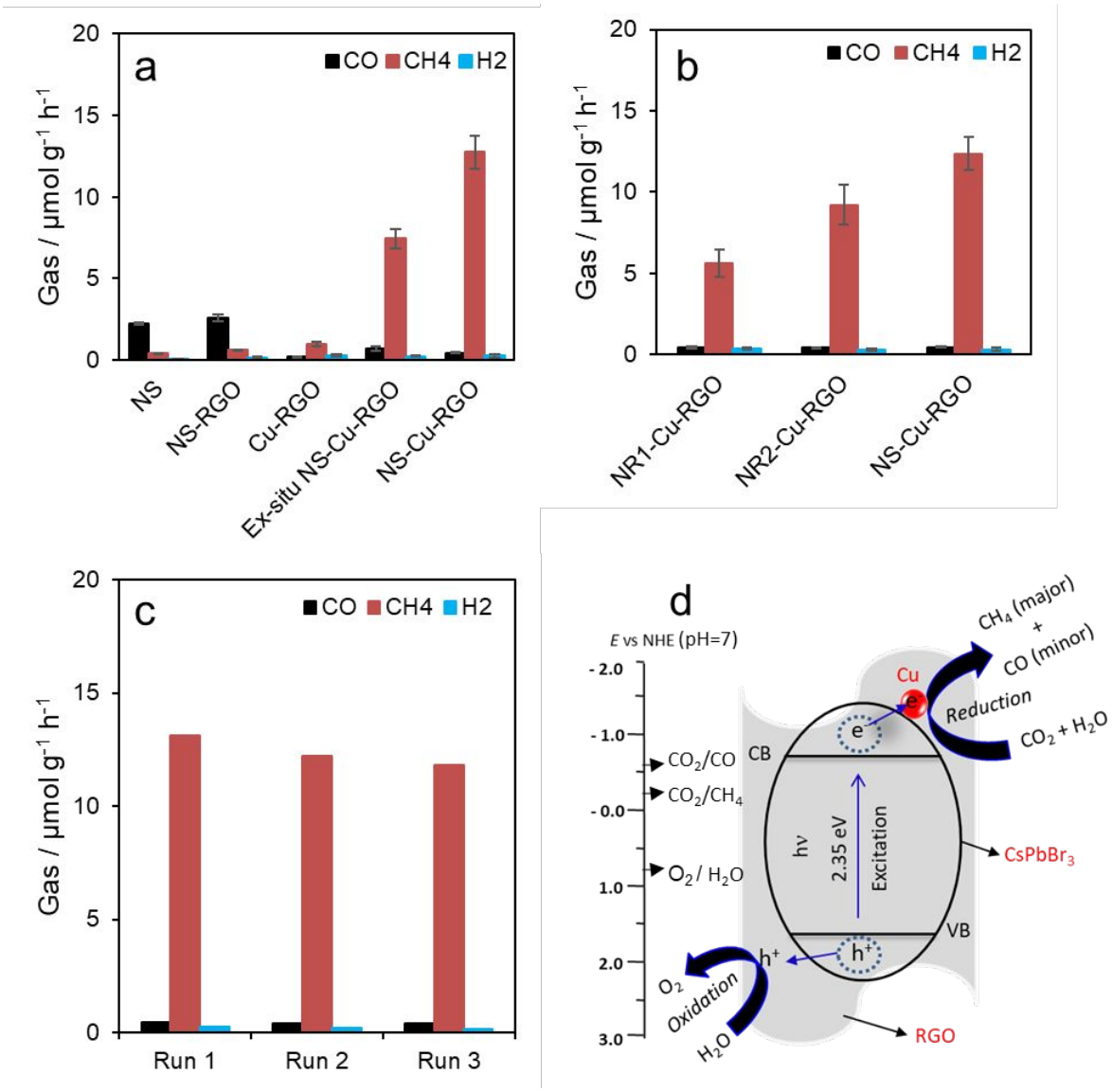

Figure 8. (a,b) CO, CH_4, and H_2 production rates by photocatalytic CO_2 + H_2O (g) conversion measured on different photocatalysts made of $CsPbBr_3$ (NS, NR1 or NR2) and Cu and/or RGO under 4 h of simulated sunlight. NS stands for $CsPbBr_3$ nanosheets prepared CsBr, $PbBr_2$, 500 rpm, 5 mm zirconia balls, and 180 min. NR1 refers to high-aspect-ratio $CsPbBr_3$ nanorods prepared with CsOAc, $PbBr_2$, 500 rpm, 15 mm zirconia balls and 60 min. NR2 refers to 30-40 nm $CsPbBr_3$ nanorods prepared with CsOAc, $PbBr_2$, 500 rpm, 5 mm zirconia balls and 180 min. (c) Stability tests. Reusability experiments on previous NS-Cu-RGO composites for three

consecutive runs. (d) Schematic diagram for the charge separation and transfer mechanism of CO_2 reduction on $CsPbBr_3$-Cu-RGO nanocomposites under simulated sunlight.

Proposed mechanism for the high performance of $CsPbBr_3$-Cu-RGO nanocomposites:

Based on the above results, a proposed mechanism is discussed to explain the synergistic effects between $CsPbBr_3$ nanosheets and Cu-RGO in NS-Cu-RGO composites that enhanced photocatalytic activity, selectivity and stability, described in **Figure 8d**. Our experiments and characterization corroborated that the photocatalytic CO_2 reduction performance including activity and product selectivity depended on (1) chemical stability, (2) light harvesting, (3) charge separation, (4) reactants adsorption and activation, and (5) band structure.[59] The components and interfaces in NS-Cu-RGO addressed all these crucial factors. (1) Chemical stability: Mixing $CsPbBr_3$ nanosheets with hydrophobic RGO created a drier environment around the $CsPbBr_3$ halide perovskite that could hamper the formation of hydrate complexes, crucial intermediates in the degradation of $CsPbBr_3$ nanosheets, in this way improving their chemical stability but without completely suppressing the required water adsorption.[60] The more hydrophobic environment also boosted the selectivity for CO_2 reduction over hydrogen evolution, as previously observed in carbon composites.[61-62] (2) Light harvesting: $CsPbBr_3$ is an excellent candidate for visible light absorption with a band gap energy of 2.35 eV, which can harvest 23% of the solar spectrum.[63] Its use in NS-Cu-RGO composites ensured absorption of the simulated sunlight. In addition, the presence of RGO and Cu nanoparticles with broad-range absorption in the visible range could induce surface plasmon resonance and further boost the photocatalysis.[64] (3) Charge separation: RGO is known to be an excellent charge carrier mediator.[65] Used in these composites, it collected and shuttled photoinduced electrons to Cu nanoparticles and we hypothesize it could also collect holes, since in a previous work we have shown holes from $CsPbBr_3$ are transported through graphitic carbon layers.[11, 65] Collecting the

photoinduced charges away from the halide perovskite, the charge carrier separation improved (that is, the electron-hole recombination decreased). Moreover, Cu nanoparticles receiving the electrons worked as co-catalysts, keeping the electrons separated from the holes. Some direct charge transfer from the halide perovskite material to the reactant gases CO_2 and $H_2O(g)$ cannot be excluded. (4) Reactants adsorption and activation: The delocalized π-conjugated binding II_3 in RGO enhanced the CO_2 adsorption via π-π conjugation interactions.[66] Cu particles in addition activated the CO_2 molecules for their reduction and improved the selectivity for carbon products, especially for CH_4.[67-69] On the other hand, the photoinduced holes reacted with water adsorbed on the surface of the halide perovskite and could also be transferred to the RGO to react especially at hydrophilic RGO defects such as edges, providing the protons the CO_2 need to form CH_4. (5) Band structure: Unlike many other semiconductors, the $CsPbBr_3$ electronic band structure offered favorable conduction and valence bands to straddle the CO_2 and H_2O redox potentials to CH_4 (and CO & H_2) and O_2. Combining all these five qualities in composites of halide perovskite nanosheets, RGO sheets and Cu nanoparticles, photocatalytic conversion of CO_2 and water vapor to CH_4 was achieved without hole scavengers.

CONCLUSIONS

We have demonstrated a fast and convenient gram-scale mechanochemical synthesis of all-inorganic orthorhombic $CsPbBr_3$ perovskite nanocrystals with control over crystal size and morphology. The perovskite nanocrystals size and properties were finely tuned by changing the mechanochemical reaction conditions including ball milling time, ball size and Cs precursor. This is a highly promising and simple methodology which avoided or minimized the use of organic solvents, only used for work-up purposes. Importantly, we have also demonstrated their use in gas-phase photocatalytic CO_2 + $H_2O(g)$ conversion to CO, CH_4, H_2 and O_2. Furthermore, forming intimate composites of $CsPbBr_3$ nanosheets with Cu-RGO had

a profound effect on the conversion and selectivity. The photocatalytic activity (total electrons consumption) increased from 8.1 (±0.13) to 103 (±0.98) μmol h^{-1} g^{-1}, and the selectivity for CH_4 increased from 42.5(±0.04) to 98.5(±0.93)%. Furthermore, the stability in humid environments drastically improved: while $CsPbBr_3$ nanosheets alone only retained 30% of its original photocatalytic activity for CO_2 + H_2O(g) conversion during three consecutive cycles, the intimate composites with Cu-RGO retained almost 90% of its original photocatalytic activity. The $CsPbBr_3$-Cu-RGO composites achieved an apparent quantum efficiency of 1.10(±0.15)% at 523 nm. We attributed such remarkable performance to the unique properties of its individual components and their synergistic combination, which resulted in increased hydrophobic character and chemical stability, solar light absorption, electron-hole separation, and adsorption and activation of CO_2, driving the CO_2 conversion without hole scavengers (just with water vapor). These results will extend the use of halide perovskites in the photocatalytic field for solar fuels, leveraging the halide perovskite unique semiconductor properties for the solar energy harvesting and CO_2 utilization.

ASSOCIATED CONTENT

Supporting Information.

Additional structural characterization, apparent quantum efficiency calculations and activity comparison with literature reports.

AUTHOR INFORMATION

Corresponding Author

* E-mail: s.eslava@imperial.ac.uk

Funding Sources

EPSRC grants EP/S030727/1, EP/S017615/1, EP/R035407/1 and EP/R035407/2.

Notes

The authors declare no competing financial interest.

ACKNOWLEDGEMENTS

Santosh Kumar and Salvador Eslava thank the EPSRC grants EP/S030727/1, EP/S017615/1, EP/R035407/1, and EP/R035407/2 for financial support.

REFERENCES

1. Faunce, T.; Styring, S.; Wasielewski, M. R.; Brudvig, G. W.; Rutherford, A. W.; Messinger, J.; Lee, A. F.; Hill, C. L.; deGroot, H.; Fontecave, M.; MacFarlane, D. R.; Hankamer, B.; Nocera, D. G.; Tiede, D. M.; Dau, H.; Hillier, W.; Wang, L.; Amal, R., Artificial photosynthesis as a frontier technology for energy sustainability. *Energy & Environmental Science* **2013,** *6* (4), 1074-1076.
2. Kamat, P. V., Meeting the Clean Energy Demand: Nanostructure Architectures for Solar Energy Conversion. *The Journal of Physical Chemistry C* **2007,** *111* (7), 2834-2860.
3. Wu, Y. A.; McNulty, I.; Liu, C.; Lau, K. C.; Liu, Q.; Paulikas, A. P.; Sun, C.-J.; Cai, Z.; Guest, J. R.; Ren, Y.; Stamenkovic, V.; Curtiss, L. A.; Liu, Y.; Rajh, T., Facet-dependent active sites of a single Cu2O particle photocatalyst for CO2 reduction to methanol. *Nature Energy* **2019,** *4* (11), 957-968.
4. Xia, P.; Zhu, B.; Yu, J.; Cao, S.; Jaroniec, M., Ultra-thin nanosheet assemblies of graphitic carbon nitride for enhanced photocatalytic CO2 reduction. *Journal of Materials Chemistry A* **2017,** *5* (7), 3230-3238.
5. Shankar, R.; Sachs, M.; Francàs, L.; Lubert-Perquel, D.; Kerherve, G.; Regoutz, A.; Petit, C., Porous boron nitride for combined CO2 capture and photoreduction. *Journal of Materials Chemistry A* **2019,** *7* (41), 23931-23940.
6. Fujiwara, H.; Hosokawa, H.; Murakoshi, K.; Wada, Y.; Yanagida, S.; Okada, T.; Kobayashi, H., Effect of Surface Structures on Photocatalytic CO2 Reduction Using Quantized CdS Nanocrystallites. *The Journal of Physical Chemistry B* **1997,** *101* (41), 8270-8278.
7. Jo, W.-K.; Kumar, S.; Eslava, S.; Tonda, S., Construction of Bi2WO6/RGO/g-C3N4 2D/2D/2D hybrid Z-scheme heterojunctions with large interfacial contact area for efficient charge separation and high-performance photoreduction of CO2 and H2O into solar fuels. *Applied Catalysis B: Environmental* **2018,** *239*, 586-598.
8. Xu, C.; Ravi Anusuyadevi, P.; Aymonier, C.; Luque, R.; Marre, S., Nanostructured materials for photocatalysis. *Chemical Society Reviews* **2019,** *48* (14), 3868-3902.

9. Li, Z.; Chen, Y.; Burda, C., Photoexcited Dynamics in Metal Halide Perovskites: From Relaxation Mechanisms to Applications. *The Journal of Physical Chemistry C* **2019,** *123* (6), 3255-3269.

10. Nayak, P. K.; Mahesh, S.; Snaith, H. J.; Cahen, D., Photovoltaic solar cell technologies: analysing the state of the art. *Nature Reviews Materials* **2019,** *4* (4), 269-285.

11. Poli, I.; Hintermair, U.; Regue, M.; Kumar, S.; Sackville, E. V.; Baker, J.; Watson, T. M.; Eslava, S.; Cameron, P. J., Graphite-protected CsPbBr3 perovskite photoanodes functionalised with water oxidation catalyst for oxygen evolution in water. *Nature Communications* **2019,** *10* (1), 2097.

12. NREL. Best Research Cell-Efficiencies. Available at: https://www.nrel.gov/pv/assets/pdfs/best-research-cell-efficiencies.20190802.pdf (National Renewable Energy Laboratory (NREL), 2019).

13. Hou, J.; Cao, S.; Wu, Y.; Gao, Z.; Liang, F.; Sun, Y.; Lin, Z.; Sun, L., Inorganic Colloidal Perovskite Quantum Dots for Robust Solar CO2 Reduction. *Chemistry – A European Journal* **2017,** *23* (40), 9481-9485.

14. Guo, S.-H.; Zhou, J.; Zhao, X.; Sun, C.-Y.; You, S.-Q.; Wang, X.-L.; Su, Z.-M., Enhanced CO2 photoreduction via tuning halides in perovskites. *Journal of Catalysis* **2019,** *369*, 201-208.

15. Xu, Y.-F.; Yang, M.-Z.; Chen, B.-X.; Wang, X.-D.; Chen, H.-Y.; Kuang, D.-B.; Su, C.-Y., A CsPbBr3 Perovskite Quantum Dot/Graphene Oxide Composite for Photocatalytic CO2 Reduction. *Journal of the American Chemical Society* **2017,** *139* (16), 5660-5663.

16. Kong, Z.-C.; Liao, J.-F.; Dong, Y.-J.; Xu, Y.-F.; Chen, H.-Y.; Kuang, D.-B.; Su, C.-Y., Core@Shell CsPbBr3@Zeolitic Imidazolate Framework Nanocomposite for Efficient Photocatalytic CO2 Reduction. *ACS Energy Letters* **2018,** *3* (11), 2656-2662.

17. Wan, S.; Ou, M.; Zhong, Q.; Wang, X., Perovskite-type CsPbBr3 quantum dots/UiO-66(NH2) nanojunction as efficient visible-light-driven photocatalyst for CO2 reduction. *Chemical Engineering Journal* **2019,** *358*, 1287-1295.

18. Wu, L.-Y.; Mu, Y.-F.; Guo, X.-X.; Zhang, W.; Zhang, Z.-M.; Zhang, M.; Lu, T.-B., Encapsulating Perovskite Quantum Dots in Iron-Based Metal–Organic Frameworks (MOFs) for Efficient Photocatalytic CO2 Reduction. *Angewandte Chemie International Edition* **2019,** *58* (28), 9491-9495.

19. Ou, M.; Tu, W.; Yin, S.; Xing, W.; Wu, S.; Wang, H.; Wan, S.; Zhong, Q.; Xu, R., Amino-Assisted Anchoring of CsPbBr3 Perovskite Quantum Dots on Porous g-C3N4 for Enhanced Photocatalytic CO2 Reduction. *Angewandte Chemie International Edition* **2018,** *57* (41), 13570-13574.

20. Swarnkar, A.; Chulliyil, R.; Ravi, V. K.; Irfanullah, M.; Chowdhury, A.; Nag, A., Colloidal CsPbBr3 Perovskite Nanocrystals: Luminescence beyond Traditional Quantum Dots. *Angewandte Chemie International Edition* **2015,** *54* (51), 15424-15428.

21. Zhang, D.; Eaton, S. W.; Yu, Y.; Dou, L.; Yang, P., Solution-Phase Synthesis of Cesium Lead Halide Perovskite Nanowires. *Journal of the American Chemical Society* **2015,** *137* (29), 9230-9233.

22. Sun, S.; Yuan, D.; Xu, Y.; Wang, A.; Deng, Z., Ligand-Mediated Synthesis of Shape-Controlled Cesium Lead Halide Perovskite Nanocrystals via Reprecipitation Process at Room Temperature. *ACS Nano* **2016,** *10* (3), 3648-3657.

23. Jodlowski, A. D.; Yépez, A.; Luque, R.; Camacho, L.; de Miguel, G., Benign-by-Design Solventless Mechanochemical Synthesis of Three-, Two-, and One-Dimensional Hybrid Perovskites. *Angewandte Chemie International Edition* **2016,** *55* (48), 14972-14977.

24. Sadhukhan, P.; Kundu, S.; Roy, A.; Ray, A.; Maji, P.; Dutta, H.; Pradhan, S. K.; Das, S., Solvent-Free Solid-State Synthesis of High Yield Mixed Halide Perovskites for Easily Tunable Composition and Band Gap. *Crystal Growth & Design* **2018,** *18* (6), 3428-3432.

25. Prochowicz, D.; Franckevičius, M.; Cieślak, A. M.; Zakeeruddin, S. M.; Grätzel, M.; Lewiński, J., Mechanosynthesis of the hybrid perovskite CH3NH3PbI3: characterization and the corresponding solar cell efficiency. *Journal of Materials Chemistry A* **2015,** *3* (41), 20772-20777.

26. Jana, A.; Mittal, M.; Singla, A.; Sapra, S., Solvent-free, mechanochemical syntheses of bulk trihalide perovskites and their nanoparticles. *Chemical Communications* **2017,** *53* (21), 3046-3049.

27. Zhu, Z.-Y.; Yang, Q.-Q.; Gao, L.-F.; Zhang, L.; Shi, A.-Y.; Sun, C.-L.; Wang, Q.; Zhang, H.-L., Solvent-Free Mechanosynthesis of Composition-Tunable Cesium Lead Halide Perovskite Quantum Dots. *The Journal of Physical Chemistry Letters* **2017,** *8* (7), 1610-1614.

28. Eslava, S.; Reynal, A.; Rocha, V. G.; Barg, S.; Saiz, E., Using graphene oxide as a sacrificial support of polyoxotitanium clusters to replicate its two-dimensionality on pure titania photocatalysts. *Journal of Materials Chemistry A* **2016,** *4* (19), 7200-7206.

29. Gonçalves, B. S.; Palhares, H. G.; Souza, T. C. C. d.; Castro, V. G. d.; Silva, G. G.; Silva, B. C.; Krambrock, K.; Soares, R. B.; Lins, V. F. C.; Houmard, M.; Nunes, E. H. M., Effect of the carbon loading on the structural and photocatalytic properties of reduced graphene oxide-TiO2 nanocomposites prepared by hydrothermal synthesis. *Journal of Materials Research and Technology* **2019,** *8* (6), 6262-6274.

30. López, R.; Gómez, R., Band-gap energy estimation from diffuse reflectance measurements on sol–gel and commercial TiO2: a comparative study. *Journal of Sol-Gel Science and Technology* **2012,** *61* (1), 1-7.

31. Li, A.; Cao, Q.; Zhou, G.; Schmidt, B. V. K. J.; Zhu, W.; Yuan, X.; Huo, H.; Gong, J.; Antonietti, M., Three-Phase Photocatalysis for the Enhanced Selectivity and Activity of CO2 Reduction on a Hydrophobic Surface. *Angewandte Chemie International Edition* **2019,** *58* (41), 14549-14555.

32. Xu, C.; De, S.; Balu, A. M.; Ojeda, M.; Luque, R., Mechanochemical synthesis of advanced nanomaterials for catalytic applications. *Chemical Communications* **2015,** *51* (31), 6698-6713.

33. Zhang, X.; Qin, J.; Xue, Y.; Yu, P.; Zhang, B.; Wang, L.; Liu, R., Effect of aspect ratio and surface defects on the photocatalytic activity of ZnO nanorods. *Scientific Reports* **2014,** *4* (1), 4596.

34. Zhou, H.; Yuan, S.; Wang, X.; Xu, T.; Wang, X.; Li, H.; Zheng, W.; Fan, P.; Li, Y.; Sun, L.; Pan, A., Vapor Growth and Tunable Lasing of Band Gap Engineered Cesium Lead Halide Perovskite Micro/Nanorods with Triangular Cross Section. *ACS Nano* **2017,** *11* (2), 1189-1195.

35. Aldibaja, F. K.; Badia, L.; Mas-Marzá, E.; Sánchez, R. S.; Barea, E. M.; Mora-Sero, I., Effect of different lead precursors on perovskite solar cell performance and stability. *Journal of Materials Chemistry A* **2015,** *3* (17), 9194-9200.

36. Introduction. In *Corrosion Handbook*. (eds G. Kreysa and M. Schütze). doi:10.1002/9783527610433.chb201003.

37. Dirin, D. N.; Cherniukh, I.; Yakunin, S.; Shynkarenko, Y.; Kovalenko, M. V., Solution-Grown CsPbBr3 Perovskite Single Crystals for Photon Detection. *Chemistry of Materials* **2016,** *28* (23), 8470-8474.

38. Butkus, J.; Vashishtha, P.; Chen, K.; Gallaher, J. K.; Prasad, S. K. K.; Metin, D. Z.; Laufersky, G.; Gaston, N.; Halpert, J. E.; Hodgkiss, J. M., The Evolution of Quantum Confinement in CsPbBr3 Perovskite Nanocrystals. *Chemistry of Materials* **2017,** *29* (8), 3644-3652.

39. Zhang, M.; Tian, Z.-Q.; Zhu, D.-L.; He, H.; Guo, S.-W.; Chen, Z.-L.; Pang, D.-W., Stable CsPbBr3 perovskite quantum dots with high fluorescence quantum yields. *New Journal of Chemistry* **2018,** *42* (12), 9496-9500.

40. Samu, G. F.; Scheidt, R. A.; Kamat, P. V.; Janáky, C., Electrochemistry and Spectroelectrochemistry of Lead Halide Perovskite Films: Materials Science Aspects and Boundary Conditions. *Chemistry of Materials* **2018,** *30* (3), 561-569.

41. Endres, J.; Egger, D. A.; Kulbak, M.; Kerner, R. A.; Zhao, L.; Silver, S. H.; Hodes, G.; Rand, B. P.; Cahen, D.; Kronik, L.; Kahn, A., Valence and Conduction Band Densities of States of Metal Halide Perovskites: A Combined Experimental–Theoretical Study. *The Journal of Physical Chemistry Letters* **2016,** *7* (14), 2722-2729.

42. Michalchuk, A. A. L.; Tumanov, I. A.; Boldyreva, E. V., Ball size or ball mass – what matters in organic mechanochemical synthesis? *CrystEngComm* **2019,** *21* (13), 2174-2179.

43. Leelavathi, A.; Madras, G.; Ravishankar, N., Origin of enhanced photocatalytic activity and photoconduction in high aspect ratio ZnO nanorods. *Physical Chemistry Chemical Physics* **2013,** *15* (26), 10795-10802.

44. Liang, Z.; Zhao, S.; Xu, Z.; Qiao, B.; Song, P.; Gao, D.; Xu, X., Shape-Controlled Synthesis of All-Inorganic CsPbBr3 Perovskite Nanocrystals with Bright Blue Emission. *ACS Applied Materials & Interfaces* **2016,** *8* (42), 28824-28830.

45. Akkerman, Q. A.; Motti, S. G.; Srimath Kandada, A. R.; Mosconi, E.; D'Innocenzo, V.; Bertoni, G.; Marras, S.; Kamino, B. A.; Miranda, L.; De Angelis, F.; Petrozza, A.; Prato, M.; Manna, L., Solution Synthesis Approach to Colloidal Cesium Lead Halide Perovskite Nanoplatelets with Monolayer-Level Thickness Control. *Journal of the American Chemical Society* **2016,** *138* (3), 1010-1016.

46. Zhang, H.; Liao, Q.; Wu, Y.; Chen, J.; Gao, Q.; Fu, H., Pure zero-dimensional Cs4PbBr6 single crystal rhombohedral microdisks with high luminescence and stability. *Physical Chemistry Chemical Physics* **2017,** *19* (43), 29092-29098.

47. Bo, Z.; Shuai, X.; Mao, S.; Yang, H.; Qian, J.; Chen, J.; Yan, J.; Cen, K., Green preparation of reduced graphene oxide for sensing and energy storage applications. *Scientific Reports* **2014,** *4*, 4684.

48. How, G. T. S.; Pandikumar, A.; Ming, H. N.; Ngee, L. H., Highly exposed {001} facets of titanium dioxide modified with reduced graphene oxide for dopamine sensing. *Scientific Reports* **2014,** *4*, 5044.

49. Reporting Physisorption Data for Gas/Solid Systems. In *Handbook of Heterogeneous Catalysis*, pp 1217-1230.

50. Wang, L.; Chen, W.; Zhang, D.; Du, Y.; Amal, R.; Qiao, S.; Wu, J.; Yin, Z., Surface strategies for catalytic CO2 reduction: from two-dimensional materials to nanoclusters to single atoms. *Chemical Society Reviews* **2019,** *48* (21), 5310-5349.

51. Ong, W.-J.; Tan, L.-L.; Chai, S.-P.; Yong, S.-T., Graphene oxide as a structure-directing agent for the two-dimensional interface engineering of sandwich-like graphene–g-C3N4 hybrid nanostructures with enhanced visible-light photoreduction of CO2 to methane. *Chemical Communications* **2015,** *51* (5), 858-861.

52. Rood, S. C.; Ahmet, H. B.; Gomez-Ramon, A.; Torrente-Murciano, L.; Reina, T. R.; Eslava, S., Enhanced ceria nanoflakes using graphene oxide as a sacrificial template for CO oxidation and dry reforming of methane. *Applied Catalysis B: Environmental* **2019,** *242*, 358-368.

53. Nayakasinghe, M. T.; Han, Y.; Sivapragasam, N.; Kilin, D. S.; Burghaus, U., Unexpected high binding energy of CO2 on CH3NH3PbI3 lead-halide organic–inorganic perovskites via bicarbonate formation. *Chemical Communications* **2018,** *54* (71), 9949-9952.

54. Tu, W.; Zhou, Y.; Liu, Q.; Yan, S.; Bao, S.; Wang, X.; Xiao, M.; Zou, Z., An In Situ Simultaneous Reduction-Hydrolysis Technique for Fabrication of TiO2-Graphene 2D Sandwich-Like Hybrid Nanosheets: Graphene-Promoted Selectivity of Photocatalytic-Driven Hydrogenation and Coupling of CO2 into Methane and Ethane. *Advanced Functional Materials* **2013,** *23* (14), 1743-1749.

55. Dey, G. R.; Belapurkar, A. D.; Kishore, K., Photo-catalytic reduction of carbon dioxide to methane using TiO2 as suspension in water. *Journal of Photochemistry and Photobiology A: Chemistry* **2004,** *163* (3), 503-508.

56. Su, Y.; Zeng, Q.; Chen, X.; Ye, W.; She, L.; Gao, X.; Ren, Z.; Li, X., Highly efficient CsPbBr3 perovskite nanocrystals induced by structure transformation between CsPbBr3 and Cs4PbBr6 phases. *Journal of Materials Chemistry C* **2019,** *7* (25), 7548-7553.

57. Yang, C.-C.; Yu, Y.-H.; van der Linden, B.; Wu, J. C. S.; Mul, G., Artificial Photosynthesis over Crystalline TiO2-Based Catalysts: Fact or Fiction? *Journal of the American Chemical Society* **2010,** *132* (24), 8398-8406.

58. Kumar, S.; Isaacs, M. A.; Trofimovaite, R.; Durndell, L.; Parlett, C. M. A.; Douthwaite, R. E.; Coulson, B.; Cockett, M. C. R.; Wilson, K.; Lee, A. F., P25@CoAl layered double hydroxide heterojunction nanocomposites for CO2 photocatalytic reduction. *Applied Catalysis B: Environmental* **2017,** *209*, 394-404.

59. Kumar, S.; Li, W.; Lee, A. F., Chapter 8 Nanocatalysts for CO2 Conversion. In *Nanoparticle Design and Characterization for Catalytic Applications in Sustainable Chemistry*, The Royal Society of Chemistry: 2019; pp 207-235.

60. Di Girolamo, D.; Dar, M. I.; Dini, D.; Gontrani, L.; Caminiti, R.; Mattoni, A.; Graetzel, M.; Meloni, S., Dual effect of humidity on cesium lead bromide: enhancement and degradation of perovskite films. *Journal of Materials Chemistry A* **2019,** *7* (19), 12292-12302.

61. Reuillard, B.; Ly, K. H.; Rosser, T. E.; Kuehnel, M. F.; Zebger, I.; Reisner, E., Tuning Product Selectivity for Aqueous CO2 Reduction with a Mn(bipyridine)-pyrene Catalyst Immobilized on a Carbon Nanotube Electrode. *Journal of the American Chemical Society* **2017,** *139* (41), 14425-14435.

62. Wang, M.; Chen, L.; Lau, T.-C.; Robert, M., A Hybrid Co Quaterpyridine Complex/Carbon Nanotube Catalytic Material for CO2 Reduction in Water. *Angewandte Chemie* **2018,** *130* (26), 7895-7899.

63. NREL, Reference Solar Spectral Irradiance: ASTM G-173. Available at https://rredc.nrel.gov/solar//spectra/am1.5/ASTMG173/ASTMG173.html

64. Lou, Z.; Fujitsuka, M.; Majima, T., Two-Dimensional Au-Nanoprism/Reduced Graphene Oxide/Pt-Nanoframe as Plasmonic Photocatalysts with Multiplasmon

Modes Boosting Hot Electron Transfer for Hydrogen Generation. *The Journal of Physical Chemistry Letters* **2017,** *8* (4), 844-849.

65. Iwase, A.; Ng, Y. H.; Ishiguro, Y.; Kudo, A.; Amal, R., Reduced Graphene Oxide as a Solid-State Electron Mediator in Z-Scheme Photocatalytic Water Splitting under Visible Light. *Journal of the American Chemical Society* **2011,** *133* (29), 11054-11057.

66. Yu, J.; Jin, J.; Cheng, B.; Jaroniec, M., A noble metal-free reduced graphene oxide–CdS nanorod composite for the enhanced visible-light photocatalytic reduction of CO2 to solar fuel. *Journal of Materials Chemistry A* **2014,** *2* (10), 3407-3416.

67. Sharma, N.; Das, T.; Kumar, S.; Bhosale, R.; Kabir, M.; Ogale, S., Photocatalytic Activation and Reduction of CO2 to CH4 over Single Phase Nano Cu3SnS4: A Combined Experimental and Theoretical Study. *ACS Applied Energy Materials* **2019**.

68. Varghese, O. K.; Paulose, M.; LaTempa, T. J.; Grimes, C. A., High-Rate Solar Photocatalytic Conversion of CO2 and Water Vapor to Hydrocarbon Fuels. *Nano Letters* **2009,** *9* (2), 731-737.

69. Kang, Q.; Wang, T.; Li, P.; Liu, L.; Chang, K.; Li, M.; Ye, J., Photocatalytic Reduction of Carbon Dioxide by Hydrous Hydrazine over Au–Cu Alloy Nanoparticles Supported on SrTiO3/TiO2 Coaxial Nanotube Arrays. *Angewandte Chemie International Edition* **2015,** *54* (3), 841-845.

TOC Graph: